Article:
Osmond, J.P.F., Zin, H.M., Harris, E.J. et al. (3 more authors) (2011) Imaging of moving fiducial markers during radiotherapy using a fast, efficient active pixel sensor based EPID. Medical Physics, 38 (11). pp. 6152-6159. ISSN 0094-2405

https://doi.org/10.1118/1.3651632

Imaging of moving fiducial markers during radiotherapy using an active pixel sensor based EPID

John P. F. Osmond,[1, a)] Hafiz M. Zin,[1] Emma J. Harris,[1] Giovanni Lupica,[2] Nigel M. Allinson,[3] and Philip M. Evans[1]

[1)] *Joint Department of Physics, The Institute of Cancer Research & The Royal Marsden NHS Foundation Trust, Downs Road, Sutton, Surrey, SM2 5PT, UK*

[2)] *Department of Electronic & Electrical Engineering, The University of Sheffield, Mappin Street, Sheffield, S1 3JD, UK*

[3)] *Lincoln School of Computer Science, University of Lincoln, Brayford Pool, Lincoln, LN6 7TS, UK*

The purpose of this work was to investigate the use of an experimental CMOS (Complementary Metal-Oxide-Semiconductor) APS (Active Pixel Sensor) for tracking of moving fiducial markers during radiotherapy. The APS has an active area of 5.4 x 5.4 cm and maximum full frame read-out rate of 20 frame s^{-1}, with the option to read out a Region-Of-Interest (ROI) at an increased rate. It was coupled to a 4 mm thick ZnWO4 scintillator which provided a quantum efficiency (QE) of 8% for a 6 MV x-ray treatment beam. The APS was compared with a standard iViewGT flat panel amorphous Silicon (a-Si) Electronic Portal Imaging Device (EPID), with a QE of 0.34% and a frame-rate of 2.5 frame s^{-1}. To investigate the ability of the two systems to image markers, four gold cylinders of length 8 mm and diameter 0.8, 1.2, 1.6 and 2 mm were placed on a motion platform. Images of the stationary markers were acquired using the APS at a frame-rate of 20 frame s^{-1}, and a dose-rate of 143 MU min^{-1} to avoid saturation. EPID images were acquired at the maximum frame-rate of 2.5 frame s^{-1}, and a reduced dose-rate of 19 MU $min^{-1}$to provide a similar dose per frame to the APS. Signal-to-Noise Ratio (SNR) of the background signal and Contrast-to-Noise Ratio (CNR) of the marker signal relative to the background were evaluated for both imagers at doses of 0.125 to 2 MU. Image quality and marker visibility was found to be greater in the APS with SNR ∼5 times greater than in the EPID and CNR up to an order of magnitude greater for all four markers. To investigate the ability to image and track moving markers the motion platform was moved to simulate a breathing cycle with period 6 s, amplitude 20 mm and maximum speed 13.2 mm s^{-1}. At the minimum integration time of 50 ms a tracking algorithm applied to the APS data found all four markers with a success rate of ≥92% and positional error ≤90 μm. At an integration time of 400 ms the smallest marker became difficult to detect when moving. The detection of moving markers using the a-Si EPID was difficult even at the maximum dose-rate of 592 MU min^{-1} due to the lower QE and longer integration time of 400 ms. This work demonstrates that a fast read-out, high QE APS may be useful in the tracking of moving fiducial markers during radiotherapy. Further study is required to investigate the tracking of markers moving in 3-D in a treatment beam attenuated by moving patient anatomy. This will require a larger sensor with ROI read-out to maintain speed and a manageable data-rate.

Keywords: image-guided radiotherapy, fiducial markers, implanted markers, tracking, complementary metal-oxide-semiconductor, active pixel sensor, electronic portal imaging

I. INTRODUCTION

Current radiotherapy techniques such as Intensity Modulated Radiation Therapy (IMRT)[1] and Volume Modulated Arc Therapy (VMAT)[2,3] are able to deliver highly conformal 3D dose distributions. However in the case of moving tumours, such as those located in the lung, the Planning Target Volume (PTV) is often defined to include the position of the tumour at all times resulting in the irradiation of healthy tissue[4]. To ameliorate this effect and improve the therapeutic ratio information describing the motion of the tumour may be used to gate the treatment[5], or possibly to adapt the delivery to account for the motion[6]. The motion of the tumour may be determined from external skin markers[7], breath monitoring[8], imaging of the MV treatment beam[9], additional keV imaging[10,11] or implanted electromagnetic markers[12,13]. The advantage of imaging the treatment beam is that it requires no correlation between organ motion and external body motion and provides a beam's eye view of the tumour relative to the collimator. The same image data can also be used to verify the beam duration, field size and position of individual collimator leaves providing a more comprehensive verification system[14,15]. However the high energy of the treatment beam results in poor contrast between soft tissues of similar density necessitating the use of high density materials such as bone or implanted Fiducial Markers (FMs) to infer tumour position[16,17]. Furthermore the poor Quantum Efficiency (QE) and slow frame-rate inherent in the current generation of MV Electronic Portal Imaging Devices (EPIDs) can make the tracking of small moving features

[a)] Electronic mail: john.osmond@icr.ac.uk

difficult, and their susceptibility to damage by MV radiation results in failure after 1-2 years.

Complementary Metal-Oxide Semiconductor (CMOS) Active Pixel Sensors (APS) are commonly used in commercial products such as digital cameras, mobile phones and webcams and recent advancements have produced sensors suitable for use in scientific applications such as medical imaging[18–20]. The addressable read-out architecture characteristic of APS sensors provides fast full frame or Region-Of-Interest (ROI) read-out and allows for the construction of small pixel and large area sensors without the corresponding decrease in frame-rate associated with a sequential read-out. The increased read-out rate also allows the use of a more efficient scintillator without an increase in the number of saturated pixels. These properties combined with the relatively low cost, low power consumption and improved radiation hardness means that APS sensors offer a potential advantage in the imaging of small, low contrast moving FMs in an MV treatment beam.

This study investigates the feasibility of using an APS sensor with high QE and fast read-out to track moving FMs. The APS sensor used was a small prototype developed by the MI^3 consortium[21]. It features an active area of 5.4 x 5.4 cm and a maximum full frame rate of 20 frame s^{-1}. Selecting a ROI within the frame increases the read-out rate but 20 frame s^{-1} was considered sufficient as it would mean a marker moving at a clinically relevant speed of up to 20 mm s^{-1} would travel less than 1 mm between frames. Gold markers of varying size were moved in 1-D according to the Lujan approximation to breathing motion and imaged using both the APS and an a-Si EPID. Image quality, marker visibility and the success of a tracking algorithm were evaluated for both technologies and a comparison made.

II. MATERIALS AND METHODS

A. Sensor and packaging

The APS sensor used in this work is referred to as the Large Area Sensor (LAS). The sensor specification is detailed in Table I along with the specification of the standard iViewGT a-Si EPID supplied with an Elekta Synergy Linac (Elekta Oncolgy Systems, Crawley, UK).

Significant modifications were required to make the APS sensor suitable for use in an MV treatment beam. Specifically, the sensor control and read-out electronics were originally situated directly behind the active sensor area and as such were at risk of damage from the incident x-ray radiation. The PCB containing these electronics was redesigned to move the electronics out of the treatment beam, and a housing constructed to exclude stray optical light whilst allowing air to flow past the sensor to improve thermal stability. A 5.4 x 5.4 cm x 4 mm thick (3048 mg cm^{-2}) $ZnWO_4$ scintillator, formed from two monolithic crystals 5.4 x 3.8 and 5.4 x 1.6 cm in size and glued to a 1 mm glass substrate, was placed directly on the sensor surface. A 1 mm copper plate was placed on the scintillator, as in the a-Si EPID. A diagram of the modified sensor is shown in Fig 1.

Table I. Basic properties of the CMOS Active Pixel Sensor (APS) and iViewGT amorphous Silicon (a-Si) Electronic Portal Imaging Device (EPID).

	APS	a-Si EPID
Pixel size	40 × 40 μm	400 × 400 μm
Detector size	5.4 × 5.4 cm	41.0 × 41.0 cm
Readout rate	20 frame s^{-1}	2.5 frame s^{-1}
Scintillator Material	$ZnWO_4$	Gd_2O_2S
Scintillator Thickness	3048 mg cm^{-2}	133 mg cm^{-2}
Quantum Efficiency	8 %	0.34 %

A Xilinx Virtex-II Pro FPGA development board (Xilinx Ltd., Weybridge, UK) was used to generate the required APS control signals and transfer images to the host computer via an optical transceiver. Operating parameters were defined and images acquired using a Matlab GUI (Mathworks Inc. Natwick, MA, USA) and image data stored in 12-bit binary format.

The characteristics of the iViewGT have been modelled using the EGSnrc/BEAMnrc Monte Carlo radiative transport package[22–25]. The model predicted that the responsivity of a 6 MV treatment beam, i.e. the percentage of incident energy that produces a signal, is 0.34%. The APS responsivity is dominated by the high QE of the $ZnWO_4$, which was calculated at 8% for the same beam (National Institute of Standards and Technology, Gaithersburg, USA).

B. Experimental setup

The purpose of this experiment was to make a direct comparison between an a-Si EPID and APS when used to image FMs moving according to breathing motion. Four gold cylinders of length 8 mm and diameter 0.8, 1.2, 1.6 and 2 mm were fixed 5 mm apart in a low-density plastic case. The markers were placed on a 10 mm thick Carbon-fibre board attached to a 3-D motion-platform used in previous work[26]. The APS sensor was placed on the treatment couch in the centre of the beam and with the couch in its lowest position, providing a Source Detector Distance (SDD) of 130 cm. The motion platform was placed such that the markers were 10 cm above the detector. The thin phantom and small object to detector distances were chosen to allow comparison of the effects of sensor characteristics such as pixel size, frame rate and QE on the success of a marker tracking routine. The a-Si EPID was mounted on the Linac gantry with a SDD fixed at 155 cm. For images acquired with the a-Si EPID the motion-platform was placed such that the markers were 10 cm above the detector. To evaluate the consequences of the small difference in geometry the APS was

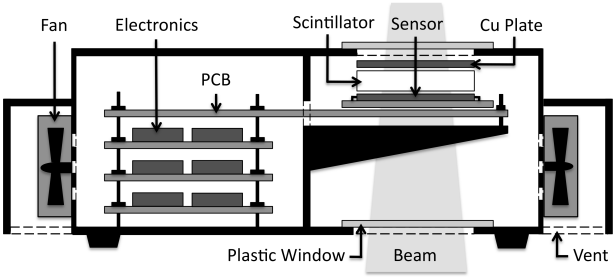

(a)

(b)

Figure 1. Diagram (a) and photo (b) showing the APS with redesigned packaging to allow use in an MV treatment beam. In (b) the housing has been opened to reveal the APS.

repositioned to an SDD = 155 cm with the markers 10 cm above. Static images of the markers were acquired and shown to be similar in quality to those obtained at an SDD = 130 cm.

To simulate the effect if in-vivo motion of the FMs the motion-platform was programmed to move in 1-D according to the Lujan approximation to breathing motion:

$$z(\mathrm{t}) = z_0 - A\cos^{2n}(\frac{\pi t}{\tau} - \theta) \qquad (1)$$

where z_0 is the position at exhale, A is the peak-to-peak amplitude of motion (20 mm), τ is the time period of the breathing cycle (6 s), n determines the shape of the distribution (set to 2) and θ is the starting phase[27]. These parameters produced a breathing cycle with speeds in the range 0 to 13.2 mm s^{-1} and a mean speed of $\bar{v} = 6.6$ mm s^{-1}. The direction of motion and the axis through the centre of the four markers were coaligned with the vertical direction in the resulting images.

C. Image acquisition and correction

To determine the optimum dose-rate for imaging using the APS a 6 MV treatment beam with a collimator aperture of 4 x 4 cm at the isocentre was applied to the motion-platform while it remained stationary. The optimum Pulse Repetition Frequency (PRF) was found to be 100, providing a dose rate of 143 MU min^{-1}. Dose rates greater than this were found to saturate a large number of pixels at the maximum full frame-rate.

A sequence of 240 frames were acquired with the APS at 20 frame s^{-1} over 12 s. A further 240 frames, equivalent to two complete breathing cycles were acquired under the same conditions but with the motion-platform moving. The procedure was repeated with the a-Si EPID running at its maximum frame-rate of 2.5 frame s^{-1} and using two dose-rates. The first was the maximum PRF of 400 (562 MU min^{-1}), and the second used a PRF of 12.5 (19 MU min^{-1}) which provided a dose within each frame comparable to the APS.

To evaluate Dark Fixed Pattern Noise (DFPN) a sequence of 240 frames were acquired with no illumination of the sensor. The mean signal was calculated for each pixel to provide a single dark frame $I_\mathrm{d}(\mathrm{x},\mathrm{y})$. To remove the effect of spatial non-uniformity in either the shape of the treatment beam or the gain of the sensor, a sequence of open images were acquired with the treatment beam applied as before and the markers removed from the field but the motion-platform and Carbon-fibre board left in place. A mean was taken to provide a single open field image $I_\mathrm{of}(\mathrm{x},\mathrm{y})$. Images of the markers acquired using both instruments were then corrected using the relation:

$$I_\mathrm{c}(\mathrm{x},\mathrm{y}) = \frac{I(\mathrm{x},\mathrm{y}) - I_\mathrm{d}(\mathrm{x},\mathrm{y})}{I_\mathrm{of}(\mathrm{x},\mathrm{y}) - I_\mathrm{d}(\mathrm{x},\mathrm{y})} \qquad (2)$$

where $I(\mathrm{x},\mathrm{y})$ is the original image and $I_\mathrm{c}(\mathrm{x},\mathrm{y})$ is the corrected image.

Previous characterisation of the APS sensor has found certain columns to exhibit a small number of spiking pixels with an unusually high signal for a short period of time[28]. The column structure is a product of the manufacturing process whereby a small number of photolithography masks are tiled to form the sensor. These spiking pixels do not significantly degrade the image quality but make the standard deviation of pixel values an inaccurate estimator of the image noise. Spiking pixels were removed by calculating the Inter-Quartile Range (IQR) of all pixel values within each sequence of frames and excluding pixels with a signal greater than the third quartile plus three times the IQR.

Images acquired with both the APS and a-Si EPID were found to contain bright vertical bars which moved uniformly across the sensor from frame to frame. These bars were a consequence of the sensors operating asynchronously with the treatment machine pulse generator. A horizontal profile of the bright bars was derived by calculating the mean value within each column in a single frame. Each row in the frame was then divided by this mean profile to remove the bars.

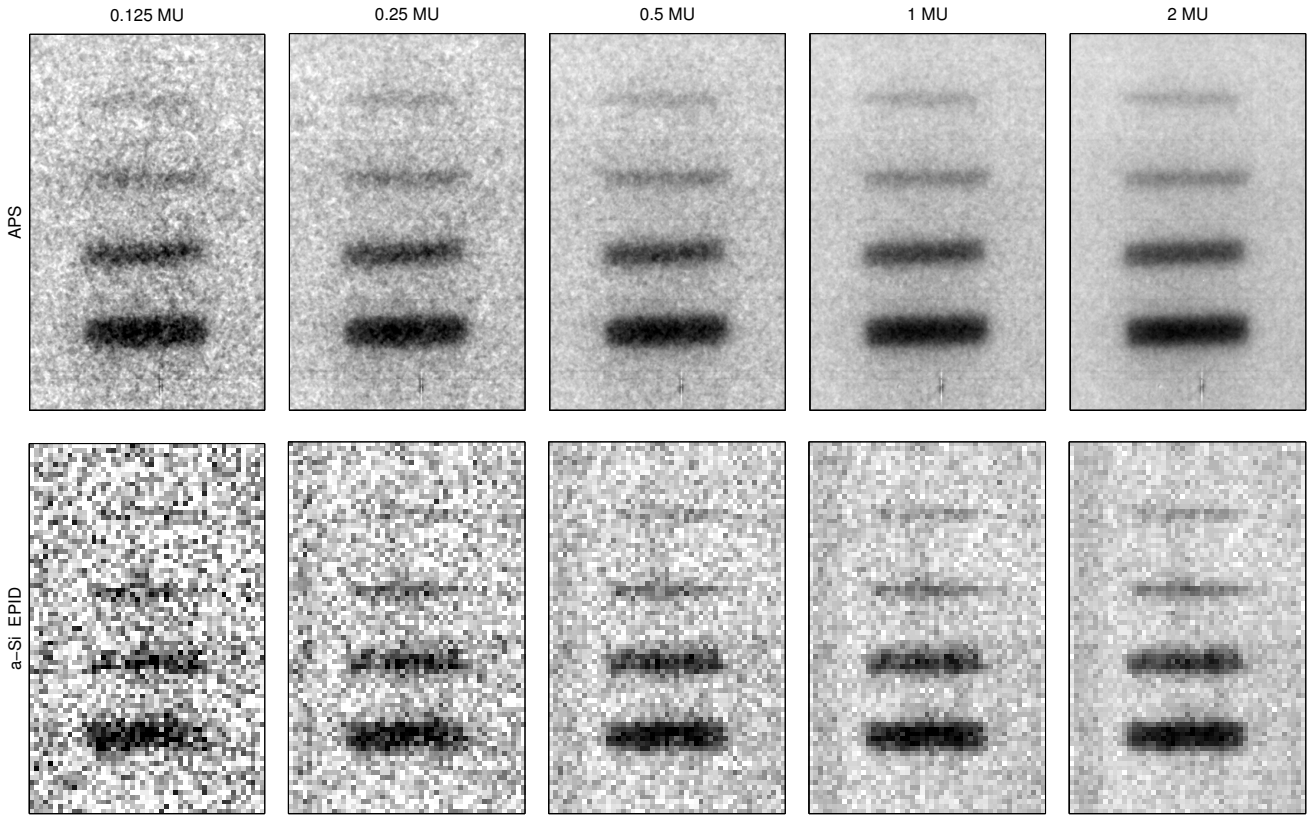

Figure 2. Four cylindrical gold markers of diameter 0.8, 1.2, 1.6 and 2 mm imaged using the 6 MV treatment beam. The top row shows images acquired using the APS at doses of 0.125 to 2 MU frame^{-1}, and the bottom row shows the same acquired using the a-Si EPID.

D. Image quality and marker visibility

To investigate the effect of dose on image quality and marker visibility two spatial regions were defined within the stationary marker frame sequence. The first region was defined so as to exclude the markers and the signal-to-noise ratio (SNR) in this region calculated using the relation:

$$SNR = \frac{\bar{I}}{\sigma_{\mathrm{I}}} \tag{3}$$

where $\bar{I}$ is the mean signal value and σ_{I} is the standard deviation. A second region containing the markers was selected and a vertical profile calculated by taking the mean row values within this region. The attenuation profiles of individual markers within the vertical profile were used to manually identify the positions of the stationary markers. To evaluate marker visibility a contrast-to-noise ratio (CNR) was calculated for each marker using the relation:

$$CNR = \frac{I_{\max} - I_{\min}}{\sigma_{\mathrm{I}}} \tag{4}$$

where $I_{\min}$ is the minimum value at the centre of each marker attenuation profile and $I_{\max}$ is the maximum value in the profile within 5 mm of the minimum position. Frames were then added together in groups of 1, 2... 20 to simulate frame-doses of 0.125, 0.25... 2 MU frame^{-1}, and SNR and CNR recalculated.

E. Automatic marker tracking

To investigate the effect of marker speed and sensor integration time on QE and the visibility of moving markers, two regions were defined in each frame of the moving marker frame sequence. The first region excluded the markers and was used to estimate frame noise, and the second contained the markers at all positions. A vertical profile was calculated for each frame from the mean row values within the marker region as before. The profile was then convolved with a kernel derived from the expected cross section of each marker in turn. The position of the four minima in the resulting convolved profiles were taken as the estimated marker positions. CNR was calculated for each marker at each position using Eqn 4. The errors in the measured marker positions were derived by plotting the position of each marker against time and

comparing with the Lujan model used to program the motion-platform. The standard deviation in the residuals from the programmed trajectory were used to estimate the error and the differential of the trajectory used to estimate marker speed. If the measured position of the marker was >2 mm from the expected position, the tracking algorithm was said to have failed, and CNR was calculated at the expected position of the marker.

Frames were then added together in groups of 1, 2... 20 to simulate integration times of 50, 100... 1000 ms in the APS, and the automatic marker tracking repeated. The distance travelled by the marker within each frame was estimated from the marker speed and the integration time for each frame. The process was repeated for the a-Si EPID.

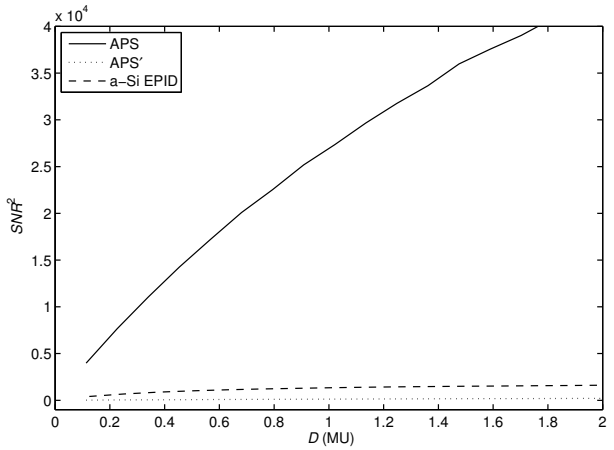

Figure 3. Square of the Signal-to-Noise Ratio (SNR^2) in the APS and a-Si EPID as a function of dose. The APS′ line corresponds to the APS result scaled to account for the difference in quantum efficiency and pixel size.

III. RESULTS AND DISCUSSION

A. Image quality and marker visibility

Fig 2 shows images of all four markers acquired with both the APS and a-Si EPID and using doses of 0.125, 0.25... 2 MU. It appears that the APS sensor provides a far superior resolution and noise at comparable dose. The smallest marker is visible to the human eye, an indicator of its visibility to an automatic tracking algorithm, at a dose of ∼0.25 MU in the APS images but requires a much larger dose of ∼1 MU before it is visible in the a-Si EPID.

Fig 3 shows the SNR vs Dose in the marker-free region of the stationary sequence for both the APS and a-Si EPID sensors. The APS provides a significantly superior image quality at comparable dose as expected from its superior QE. In addition the a-Si EPID pixels are 100 times greater in area than those in the APS leading to an averaging of signal and a corresponding reduction in noise at the expense of resolution. To estimate the reduction in noise due the increase in pixel area, APS pixels were added together to create virtual pixels of 400 x 400 μm and SNR recalculated. An estimate of SNR as a function of dose for the APS sensor but accounting for the difference in scintillator (by scaling QE) and pixel size is included as a dotted line in Fig 3 and lies below that for the a-Si EPID, suggesting that the increase in image quality is the result of the increased scintillator efficiency. However the use of more efficient scintillator with the APS sensor is possible due to the increased frame-rate.

Fig 4 shows CNR for the four stationary markers in the APS (a) and a-Si EPID (b) images as a function of dose. Both plots show the same range in dose and the range in CNR is ten times greater in the APS plot. The APS sensor provides a superior marker visibility at a comparable dose.

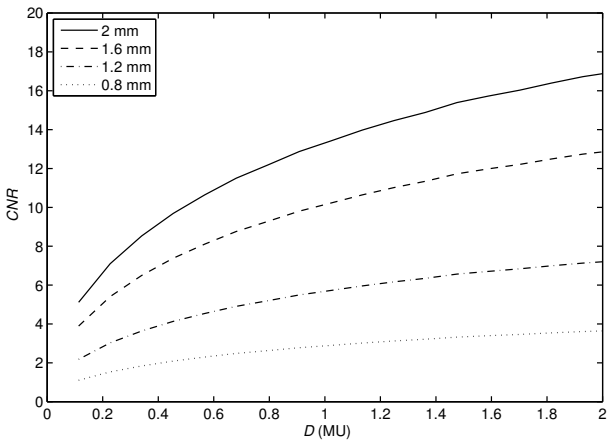

(a) APS

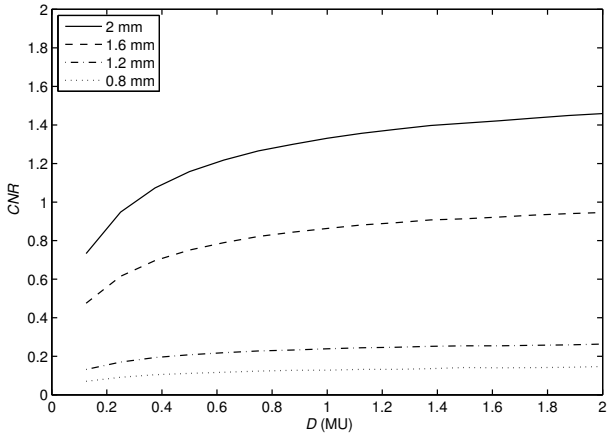

(b) a-Si EPID

Figure 4. Contrast-to-Noise Ratio (CNR) of the four static markers as a function of dose for the APS (a) and a-Si EPID (b).

B. Automatic marker tracking

Fig 5 shows the position of the four markers whilst moving, as determined by an automatic tracking algorithm applied to the APS data as a function of time. Symbols represent the measured positions, and the lines correspond to the positions expected from the input to the motion-platform. The positions are shown for two integration times, 100 ms (a) corresponding to twice the minimum integration time of the APS and 400 ms (b) equivalent to the minimum integration time of the a-Si EPID. Data corresponding to the minimum APS integration time of 50 ms is not shown as the quantity of measurements makes the resulting plot difficult to interpret. At $t_\mathrm{i} = 100$ ms integration time almost all markers are successfully located at all times and the measured positions agree well with expectation. For 400 ms only the 2 mm marker is accurately located at all times. The smaller markers are well located while stationary but are increasingly poorly located with decreasing marker size when moving. This may be the result of a marker travelling further in one integration time and spreading its attenuation signal over a larger number of pixels with a corresponding drop in CNR, despite the drop in noise resulting from the longer integration time. This would make it more difficult to both locate the marker amongst the noise, and accurately determine the centre of its attenuation profile.

To further illustrate the effect of integration time on the effectiveness of the automatic tracking algorithm as applied to the APS data, Fig 6(a) shows the success rate as a function of integration time and for each of the four markers. Fig 6(b) shows the error in the measured position. The solid vertical lines represent the minimum integration times of the APS and a-Si EPID. At the APS integration time the three largest markers are located with a success rate of 100%, and error of 40, 49 and 59 μm in decreasing order of marker size, which is close to the pixel size of the APS (40 μm). The smallest 0.8 mm marker is detected with a success rate of 92% and error of 90 μm. However at the a-Si EPID minimum integration time the success rate has dropped below 100% for all four markers and the two smallest markers are located with a success rate of 71% and 46%, and errors of 0.54 and 0.41 mm. All errors are small relative to the breathing amplitude of 20 mm suggesting that success rate may be a more appropriate indicator of the quality of the automatic tracking.

The relationship between CNR and the success rate in tracking is shown in Fig 7. Success is calculated using all four markers imaged at all integration times and measurements are grouped according to CNR into twenty evenly spaced bins, each containing >20 markers.

Fig 8 shows the effect of marker speed and integration time on detectability. The x-axis (Δ_s) denotes the distance a marker travels in a single frame. Markers were grouped together according to Δ_s into 7 evenly spaced bins between 0 and 3.5 mm. The mean and standard deviation of CNR within these bins is shown. CNR appears to drop with increasing Δ_s for all four markers and the smallest marker only exhibits a CNR significantly above 1 for Δ_s below 1.5 mm. Given a maximum marker speed of 13.2 mm s^{-1}, the longest integration time required to limit travel to below 1.5 mm is 114 ms, corresponding to a frame-rate of 8.8 frame s^{-1}.

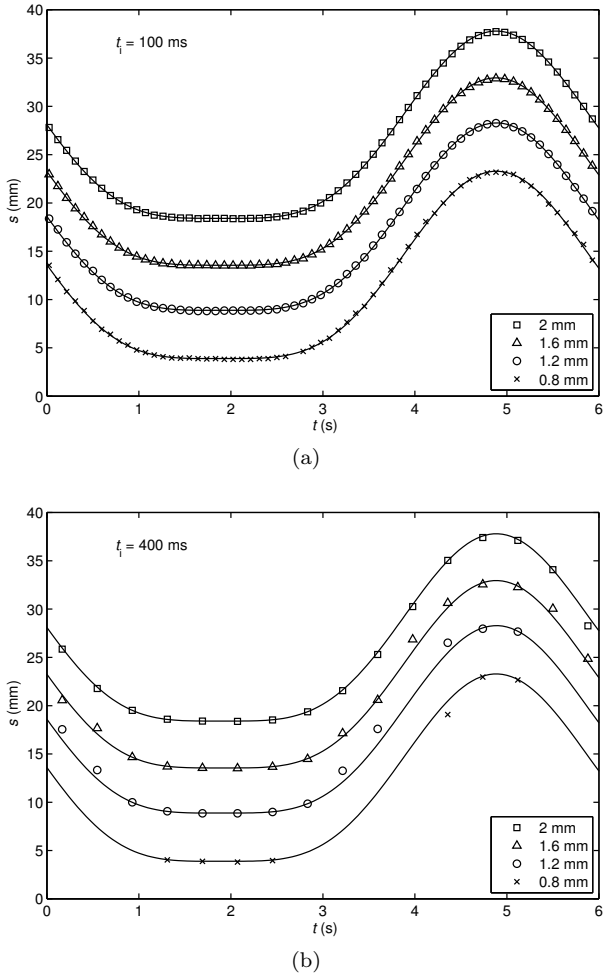

Figure 5. Positions of the four markers as a function of time. The symbols represent the marker positions as found by the tracking algorithm applied to the APS data and the solid lines represent the expected positions. Fig (a) corresponds to an integration time of 100 ms and (b) to 400 ms.

When applied to the a-Si EPID data the tracking algorithm was unable to locate the moving markers except in the case of stationary or very slow moving markers imaged using the minimum integration time of 400 ms. Fig 9 shows two typical marker attenuation profiles for both the slow moving region of the breathing cycle, and at the mean speed of 6.6 mm s^{-1}. Marker positions can be easily derived from the slow moving profile, however the speed of the marker combined with the relatively long integration time of the a-Si EPID results in the profiles of the four moving markers blurring together and appearing

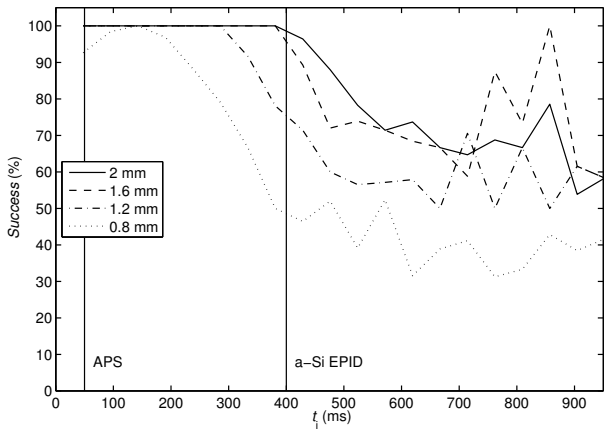

(a)

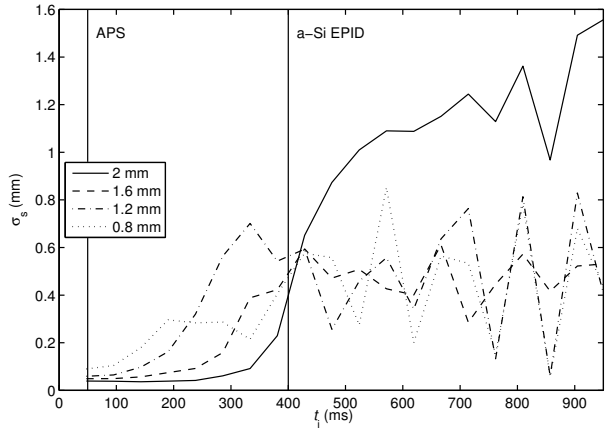

(b)

Figure 6. The success of the tracking algorithm applied to the APS data for the four markers as a function of integration time. Fig (a) shows the percentage of markers found to be within 2 mm of the expected position and (b) shows the error in the position of the marker. The vertical lines correspond to the minimum integration time of the APS and a-Si EPID.

indistinct.

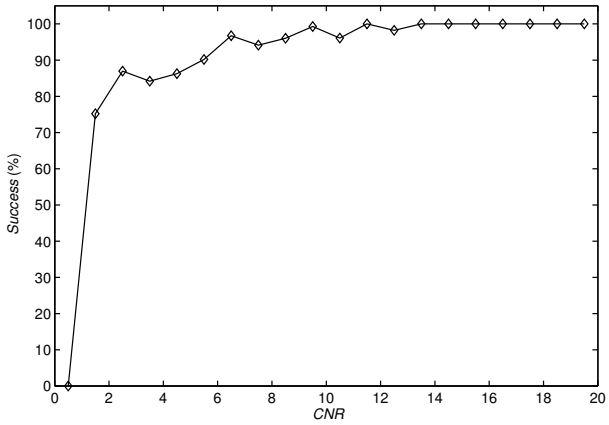

Figure 7. Success of the tracking algorithm applied to the APS data as a function of CNR. Success is the percentage of markers found to be within 2 mm of their expected position. Markers are grouped according to CNR in 20 evenly spaced bins.

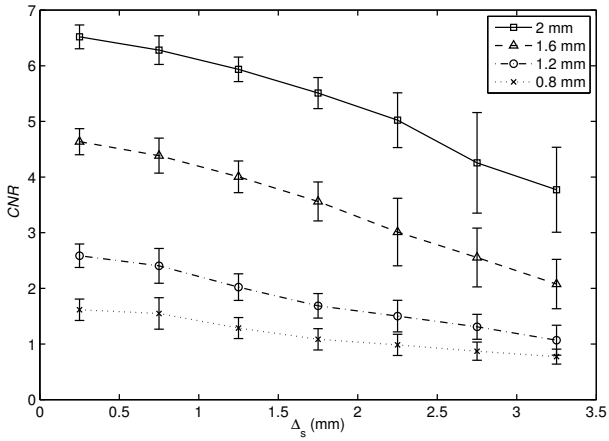

Figure 8. CNR of the four markers as a function of distance travelled within an APS frame. Values are averaged within 7 evenly spaced bins containing >20 values. Error-bars correspond to 1 standard deviation.

IV. CONCLUSIONS

This work has demonstrated the use of a high quantum efficiency, fast readout CMOS active pixel sensor for imaging moving fiducial markers during radiotherapy. The APS can image markers with greater contrast-to-noise ratio than the conventional flat panel a-Si EPID at an equivalent dose. At its fastest frame-rate of 20 frame s^{-1} the APS can track the smallest 0.8 mm marker when moving at up to 13.2 mm s^{-1} with a success rate of 92% and a positional error of 90 μm. The three larger makers are located with a success rate of 100% and positional error of 40-60 μm at the same frame-rate. The slow frame-rate of the a-Si EPID results in an attenuation profile that is too blurred to determine the positions of moving markers. The preliminary results presented here were obtained with markers moving in 1-D, placed close to the imagers and with no intervening absorber. This allowed for a direct comparison between the performance of the two imaging systems. To better replicate in-vivo conditions the markers should be moved in 3-D and imaged with an intervening moving anatomical phantom and this will be the subject of future work. The APS used here is an experimental model and too small for routine clinical use (5.4 x 5.4 cm). A larger sensor (12 x 12 cm) is under development that will allow ROI readout at 45 frame s^{-1}.

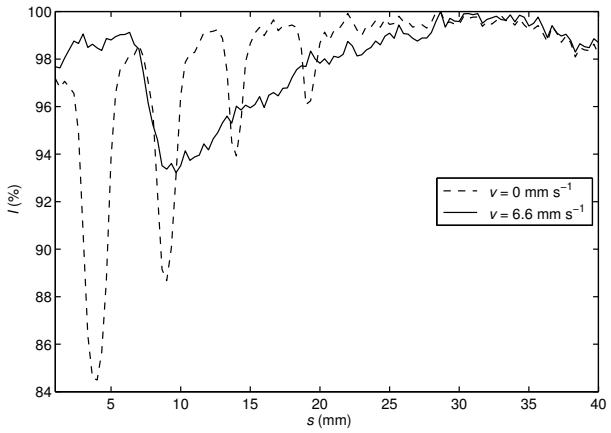

Figure 9. Attenuation profiles of the four markers moving at two speeds using the a-Si EPID. Images were acquired using the maximum Pulse Repetition Frequency of 400 s^{-1} and the minimum integration time of 400 ms.

V. ACKNOWLEDGEMENTS

This work was supported by The Engineering and Physical Sciences Research Council under grants GR/S85733/01, EP/F035985/1 and EP/F038518/1. Research at The Institute of Cancer Research is also supported by Cancer Research UK under Programme C46/A10588 and NIHR funding to the Biomedical Research Centre. The authors would like to thank Chris Bunton and Peter Clowes (The Institute of Cancer Research & The Royal Marsden NHS Trust) for their help with this work.

REFERENCES

[1] D. J. Convery and M. E. Rosenbloom, "The generation of intensity-modulated fields for conformal radiotherapy by dynamic collimation," Phys. Med. Biol., **37**, 1359–1374 (1992).

[2] C. X. Yu, "Intensity-modulated arc therapy with dynamic multileaf collimation: an alternative to tomotherapy," Phys. Med. Biol., **40**, 1435–1449 (1995).

[3] K. Otto, "Volumetric modulated arc therapy: IMRT in a single gantry arc," Med. Phys., **35**, 310–317 (2008).

[4] M. V. Herk, "Errors and margins in radiotherapy," Semin. Radiat. Oncol., **14**, 52–64 (2004).

[5] H. D. Kubo and B. C. Hill, "Respiration gated radiotherapy treatment: A technical study," Phys. Med. Biol., **41**, 83–91 (1996).

[6] D. McQuaid and S. Webb, "IMRT delivery to a moving target by dynamic MLC tracking: delivery for targets moving in two dimensions in the beam's eye view," Phys. Med. Biol., **51**, 4819–4839 (2006).

[7] D. P. Gierga, J. Brewer, G. C. Sharp, M. Betke, C. G. Willett, and G. T. Y. Chen, "The correlation between internal and external markers for abdominal tumors: Implications for respiratory gating," Int. J. Radiat. Onc. Biol. Phys., **61**, 1551–1558 (2005).

[8] L. Simon, P. Giraud, V. Servois, and J. C. Rosenwald, "Lung volume assessment for a cross-comparison of two breathing-adapted techniques in radiotherapy," Int. J. Radiat. Onc. Biol. Phys., **63**, 602–609 (2005).

[9] P. J. Keall, A. D. Todor, S. S. Vedam, C. L. Bartee, J. V. Siebers, V. R. Kini, and R. Mohan, "On the use of EPID-based implanted marker tracking for 4D radiotherapy," Med. Phys., **31**, 3492–3499 (2004).

[10] H. Shirato, S. Shimizu, K. Kitamura, T. Nishioka, K. Kagei, S. Hashimoto, H. Aoyama, T. Kunieda, N. Shinohara, H. Dosaka-Akita, and K. Miyasaka, "Four-dimensional treatment planning and fluoroscopic real-time tumor tracking radiotherapy for moving tumor," Int. J. Radiat. Onc. Biol. Phys., **48**, 435–442 (2000).

[11] H. Shirato, S. Shimizu, T. Kunieda, K. Kitamura, M. V. Herk, K. Kagei, T. Nishioka, S. Hashimoto, K. Fujita, H. Aoyama, K. Tsuchiya, K. Kudo, and K. Miyasaka, "Physical aspects of a real-time tumor-tracking system for gated radiotherapy," Int. J. Radiat. Onc. Biol. Phys., **48**, 1187–1195 (2000).

[12] T. R. Willoughby, P. A. Kupelian, J. Pouliot, K. Shinohara, M. Aubin, M. Roach, L. L. Skrumeda, J. M. Balter, D. W. Litzenberg, S. W. Hadley, J. T. Wei, and H. M. Sandler, "Target localization and real-time tracking using the Calypso 4D localization system in patients with localized prostate cancer," **65**, 528–534 (2006).

[13] P. Kupelian, T. Willoughby, A. Mahadevan, T. Djemil, G. Weinstein, S. Jani, C. Enke, T. Solberg, N. Flores, D. Liu, D. Beyer, and L. Levine, "Multi-institutional clinical experience with the Calypso system in localization and continuous, real-time monitoring of the prostate gland during external radiotherapy," Int. J. Radiat. Onc. Biol. Phys., **67**, 1088–1098 (2007).

[14] M. Partridge, P. M. Evans, A. Mosleh-Shirazi, and D. J. Convery, "Independent verification using portal imaging of intensity-modulated beam delivery by the dynamic mlc technique," Med. Phys., **25**, 1872–1879 (2008).

[15] J. P. F. Osmond, E. J. Harris, A. T. Clark, R. J. Ott, A. D. Holland, and P. M. Evans, "An investigation into the use of CMOS active pixel technology in image-guided radiotherapy," Phys. Med. Biol., **53**, 3159–3174 (2008).

[16] E. J. Harris, H. A. McNair, and P. M. Evans, "Feasibility of fully automated detection of fiducial markers implanted into the prostate using electonic portal imaging: A comparison of methods," **66**, 1263–1270 (2006).

[17] R. D. Wiersma, W. Mao, and L. Xing, "Combined kV and MV imaging for real-time tracking of implanted fiducial markers," Med. Phys., **35**, 1191–1198 (2008).

[18] S. E. Bohndiek, E. J. Cook, C. D. Arvanitis, A. Olivo, G. J. Royle, A. T. Clark, M. L. Prydderch, R. Turchetta, and R. D. Speller, "A CMOS active pixel sensor system for laboratory-based x-ray diffraction studies of biological tissue," Phys. Med. Biol., **581**, 655–672 (2008).

[19] J. Cabello, A. Bailey, I. Kitchen, M. Prydderch, A. Clark, R. Turchetta, and K. Wells, "Digital autoradiography using room temperature CCD and CMOS imaging technology," Phys. Med. Biol., **52**, 4993–5011 (2007).

[20] A. Olivo, C. D. Arvanitis, S. J. Bohndiek, A. T. Clark, R. Turchetta, and R. D. Speller, "First evidence of phase contrast imaging with laboratory sources and active pixel sensors," Nucl. Instr. and Meth., **581**, 776–782 (2007).

[21] N. Allinson, T. Anaxagoras, J. Aveyard, C. Arvanitis, R. Bates, A. Blue, S. Bohndiek, J. Cabello, L. Chen, S. Chen, A. Clark, C. Clayton, E. Cook, A. Cossins, J. Crooks, M. El-Gomati, P. M. Evans, W. Faruqi, M. French, J. Gow, T. Greenshaw, T. Greig, N. Guerrini, E. J. Harris, R. Henderson, A. Holland, G. Jeyasundra, D. Karadaglic, A. Konstantinidis, H. X. Liang, K. M. S. Maini, G. McMullen, A. Olivo, V. O'Shea, J. Osmond, R. J. Ott, M. Prydderch, L. Qiang, G. Riley, G. Royle, G. Segneri, R. Speller, J. R. N. Symonds-Tayler, S. Triger, R. Turchetta, C. Venanzi, K. Wells, X. Zha, and H. Zin, "The multidimensional integrated intelligent imaging project (MI-3)," Nucl. Instr. and Meth., **604**, 196–198 (2009).

[22] W. Nelson, D. W. O. Rogers, and H. Hirayama, "The EGS4 code system, stanford linear accelerator center report SLAC-265," (Stanford, CA: SLAC) (1985).

[23]D. W. Rogers, B. A. Faddagon, G. X. Ding, C. M. Ma, J. We, and T. R. Mackie, "BEAM: A Monte Carlo code to simulate radiotherapy treatment units," , 502–524 (1995).

[24]L. Parent, J. Seco, P. M. Evans, A. Fielding, and D. R. Dance, "Monte Carlo modelling of a a-si EPID response: the effect of spectral variations with field size and position," Med. Phys., **33**, 4527–4540 (2006).

[25]D. A. Roberts, V. N. Hansen, A. C. Niven, M. G. Thompson, J. Seco, and P. M. Evans, "A low z linac and flat panel imager: Comparison with the conventional imaging approach," , 6305–6319 (2008).

[26]E. Nioutsikou, J. R. N. Symonds-Tayler, J. L. Bedford, and S. Webb, "Quantifying the effect of respiratory motion on lung tumour dosimetry with the aid of a breathing phantom with deforming lungs," Phys. Med. Biol., **51**, 3359–3374 (2006).

[27]A. E. Lujan, E. W. Larsen, J. M. Balter, and R. K. T. Haken, "A method for incorporating organ motion due to breathing into 3D dose calculations," Med. Phys., **26**, 715–720 (1999).

[28]H. M. Zin, A. C. Konstantinidis, E. J. Harris, J. P. F. Osmond, A. Olivo, S. E. Bohndiek, A. T. Clark, R. Turchetta, N. Guerrini, J. Crooks, N. M. Allinson, R. Speller, and P. M. Evans, "Characterisation of regional variations in a stitched CMOS active pixel sensor," Nucl. Instr. and Meth., **620**, 540–548 (2010).